Ab initio static and molecular dynamics study of the absorption spectra of the 4-styrylpyridine photoswitch in its *cis* and *trans* forms†

Latévi Max Lawson Daku,*[a] Jorge Linares[b] and Marie-Laure Boillot[c]

Received 7th October 2009, Accepted 19th February 2010
First published as an Advance Article on the web 13th April 2010
DOI: 10.1039/b920850j

We report a thorough investigation of the absorption spectra of the *cis* and *trans* isomers of the 4-styrylpyridine photoswitch based on TDDFT calculations. The spectra of both isomers were analysed first from the results of excitation calculations performed on their optimised geometries. The main absorption band of the *cis* isomer is thus predicted to be due to the $S_0 \rightarrow S_1$ and $S_0 \rightarrow S_2$ transitions, while the main absorption band of the *trans* isomer is predicted to originate exclusively from the $S_0 \rightarrow S_1$ transition. The convolution of the calculated oscillator strengths with Gaussians helped mimic the broadening of the electronic transitions. However, it proved necessary to use Gaussians with a large full width at half maximum of 5000 cm^{-1}; and, compared to experiment, the calculated main absorption bands of the two isomers are significantly red-shifted and far too symmetric. Consequently, as required for the detailed analysis of the finite-temperature absorption spectrum of a molecule as flexible as 4-styrylpyridine, the influence of the thermal fluctuations has been taken into account by calculating the spectra as time averages over Car–Parrinello molecular dynamics trajectories. For both isomers, this led to a noticeable improvement in the relative positions of the calculated and experimental main absorption bands, and the asymmetry of the calculated bands brings them in better agreement with the experimental ones. Furthermore, these last results show that, actually, the $S_0 \rightarrow S_1$ and $S_0 \rightarrow S_2$ transitions both contribute significantly to the finite-temperature main absorption bands of the two isomers. Finally, in order to also take the vibrational broadening into account, the Franck–Condon factors of the relevant vibrations were calculated within the displaced harmonic oscillator approximation. By thus taking both the thermal and the vibrational broadening into account for the calculation of the absorption bands, the agreement between experiment and theory could be further improved.

1. Introduction

The photophysics of the photoisomerisable styrylpyridines, *i.e.* the aza-analogues of stilbene, has been actively investigated for several decades.[1–6] The presence of the N heteroatom enables their use as ligands in transition metal complexes. The photo-induced *cis* ⇆ *trans* isomerisation of the styrylpyridines can then serve as a means for photoswitching the properties of the complexes. The photocontrol of the reactivity of porphyrin complexes could be achieved in this way.[7–9] The ligand-driven light-induced spin change (LD-LISC) phenomenon[10–14] results from the application of this approach to complexes of first-row transition metal cations, such as Fe(II) or Fe(III), which can exhibit spin crossover.[15–17] In this phenomenon, the optical switching of the photoreactive ligand—namely, the *cis* ⇆ *trans* photoisomerisation of 4-styrylpyridine—causes a change of electronic structure which in turn may induce the high-spin ↔ low-spin conversion. An in-depth understanding of the LD-LISC phenomenon could be obtained from the theoretical study of LD-LISC complexes within density functional theory (DFT).[18,19] However, prior to such a study, we aim at achieving an accurate characterisation of the 4-styrylpyridine ligand using DFT methods.

We thus recently reported the detailed DFT study of the photoisomerisable 4-styrylpyridine in its S_0 ground state.[20] The *trans* isomer of planar geometry was shown to be the most stable isomer with a *cis–trans* zero-point energy difference of ΔE^0_{CT} = 1680 cm^{-1}. Furthermore, *ab initio* molecular dynamics (AIMD) simulations performed at 50, 150 and 300 K using the Car–Parrinello (CP) scheme[21] allowed us to evidence the highly flexible nature of the molecule in the two conformations. The evolution of the molecule in the vicinity of the *cis* and *trans* minima was indeed found to be characterised by large fluctuations whose amplitude increases with the temperature. In particular, from the point of view of an observer sitting on the ethylenic fragments, the phenyl and pyridinyl moieties undergo large and concerted clockwise–anticlockwise partial rotations about the single C–C bonds. It especially follows from these simulations that the *trans* isomer mainly exists at finite temperatures in a nonplanar form.

[a] *Faculté des Sciences, Université de Genève, 30 quai Ernest-Ansermet, CH-1211 Genève 4, Switzerland. E-mail: max.lawson@unige.ch*
[b] *Groupe d'Etude de la Matière Condensée, UMR 8635, Université de Versailles Saint-Quentin-en-Yvelines, 45 Avenue des Etats-Unis, 78035 Versailles Cedex, France*
[c] *Institut de Chimie Moléculaire et des Matériaux d'Orsay, UMR 8182, Equipe de Chimie Inorganique, Université Paris-Sud 11, 15 rue G. Clémenceau, 91405 Orsay Cedex, France*

† Electronic supplementary information (ESI) available: The results of vibration analyses, calculated Huang–Rhys factors, and the B3LYP/$\mathcal{G}$ S_1 geometry of the *cis* isomer. See DOI: 10.1039/b920850j

With the present study, we extend our previous *ab initio* static and dynamic study of the photoswitchable 4-styrylpyridine molecule to the absorption spectra of its isomers.

2. Computational details

The ground-state electronic absorption spectra of the two isomers of 4-styrylpyridine were analysed on the basis of electronic excitation calculations performed with the NWChem program package[22,23] within linear response in time-dependent DFT (LR-TDDFT)[24] using the B3LYP(AC) exchange–correlation (XC) potential[25] and the Gaussian-type orbital (GTO) basis set $\mathscr{G}'$. $\mathscr{G}'$ consists of the DFT basis set "DZVP"[26] of double-ζ polarised quality for the H atom, and of the DFT basis set "TZVP"[26] of triple-ζ polarised quality for the N and C atoms. The ground-state geometries of the two isomers used for the LR-TDDFT calculations have been reported in ref. 20: these are the optimised B3LYP/$\mathscr{G}'$ geometries and also (see below) sample configurations taken from the CPMD simulations. In order to evaluate Franck–Condon factors within the displaced harmonic oscillator approximation, we have characterised the vibrational properties of the two isomers in the S_0 ground state as well as their equilibrium geometries in the S_1 and S_2 excited states. To this end, we used the GAMESS package[27–29] because of the availability in this package of analytical TDDFT nuclear gradients.[30] The B3LYP[31–33] functional was employed in combination with the GTO $\mathscr{G}$ basis set, which consists in the GTO Dunning–Hay basis set of double-ζ quality[34] augmented with a set of polarisation functions. For these calculations, we also used the BOP functional which combines the Becke's 1988 exchange functional[35] and the one-parameter progressive correlation functional.[36] The optimisations and frequency analyses were performed with the symmetry constrained to C_s for the *trans* isomer and with no symmetry constraint for the *cis* isomer. Molecular visualisation were done with the Ecce program suite[37] and the Jmol program.[38,39]

3. Results and discussion

We first deal with the analysis of the absorption spectra of the *cis* and *trans* isomers of 4-styrylpyridine from the results of the LR-TDDFT calculations carried out at the B3LYP(AC)/$\mathscr{G}'$ level on the B3LYP/$\mathscr{G}'$ optimised geometries reported in ref. 20. Then, besides this "static" approach, we make use of the previously published results of CPMD simulations[20] to get further insight into the photophysics of the two isomers.

3.1 The "static" approach to the analysis of the absorption spectra of the isomers

Fig. 1 shows the absorption spectra of the two isomers of 4-styrylpyridine recorded in CH_3OH at room temperature. The lowest-energy absorption band of each isomer is broad and intense. The photoexcitation of the molecule in this band allows reversible switching from one isomer to the other. Upon the *trans* → *cis* isomerisation, this absorption band is shifted toward higher energies by ~3000 cm^{-1}. It also becomes broader and has its intensity reduced by a factor of about three. These features are satisfactorily reproduced by

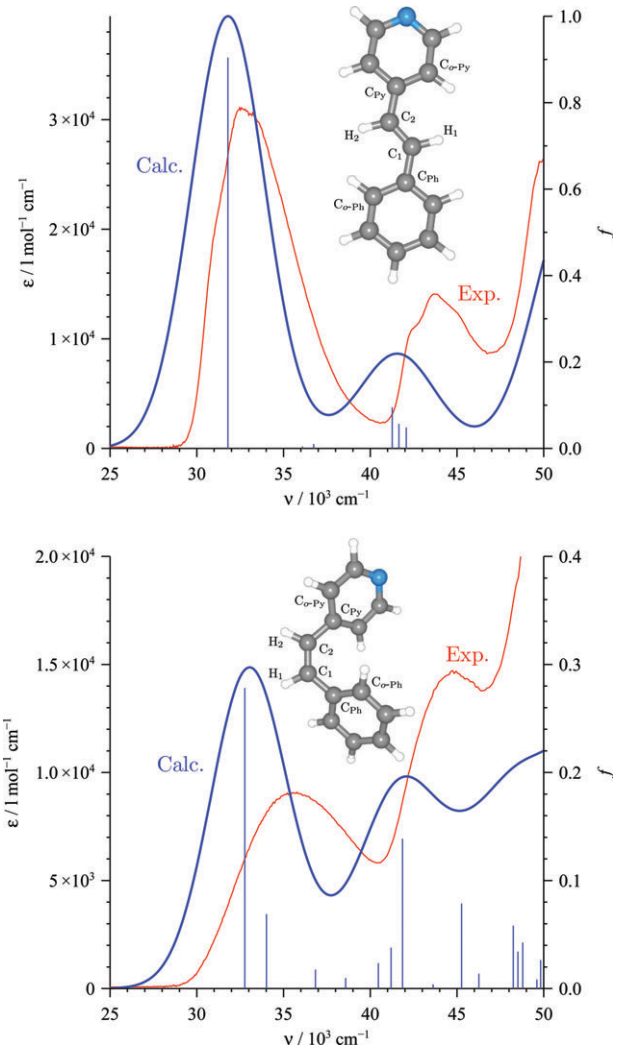

Fig. 1 Simulated (blue line) and experimental (red line) electronic absorption spectra of the *trans* (top) and *cis* (bottom) isomers of 4-styrylpyridine (the atom labelling used is also given). The calculated transition energies and oscillator strengths *f* are shown as stick-plots. The simulated spectra have been obtained by convoluting the oscillator strengths with Gaussians with a full width at half maximum of 5000 cm^{-1}.

the simulated spectra shown in Fig. 1 along with the transition energies and oscillator strengths. As compared to the experimental curves, the calculated absorption profiles exhibit a slight red shift and, for both isomers, a second absorption band is also predicted at approximately 42 000 cm^{-1}. This second band is effectively observed, at a slightly higher energy.

Tables 1 and 2 give the calculated energies and oscillator strengths of the lowest-lying spin-allowed transitions that contribute to the absorption spectra of the two conformers shown in Fig. 1. The assignments of these transitions are also reported in the two Tables. They were made on the basis of the Kohn–Sham (KS) molecular orbital (MO) diagrams of Fig. 2 and 3, which have been used to identify the major MO → MO excitations involved in the different transitions. For the *trans* isomer, these results indicate that the low-energy absorption band is mainly due to the S_0 → S_1 transition

Table 1 Results of LR-TDDFT calculations for the ten lowest-lying excited singlet states of *trans*-4-styrylpyridine: excitation energy E (cm^{-1}), oscillator strength f and assignment; (the calculations were performed on the optimised B3LYP/$\mathscr{G}'$ geometry)

	E	f	Major MO → MO transitions	Main character
$S_1(^1A')$	31794	0.90418	$48a'' \rightarrow 49a''$ (99%)	π–π*
$S_2(^1A'')$	32486	0.00153	$47a' \rightarrow 49a''$ (93%)	*n*–π*
$S_3(^1A')$	36095	0.00442	$46a'' \rightarrow 49a''$ (73%) $48a'' \rightarrow 50a''$ (22%)	CT
$S_4(^1A')$	36742	0.01011	$45a'' \rightarrow 49a''$ (75%) $48a'' \rightarrow 51a''$ (18%)	CT
$S_5(^1A'')$	40848	0.00008	$47a' \rightarrow 51a''$ (73%) $47a' \rightarrow 50a''$ (25%)	*n*–π*
$S_6(^1A')$	41269	0.09498	$48a'' \rightarrow 50a''$ (58%) $46a'' \rightarrow 49a''$ (17%) $44a'' \rightarrow 49a''$ (10%) $48a'' \rightarrow 52a''$ (8%)	CT
$S_7(^1A')$	41652	0.05661	$48a'' \rightarrow 51a''$ (66%) $45a'' \rightarrow 49a''$ (17%)	CT
$S_8(^1A')$	42080	0.04831	$44a'' \rightarrow 49a''$ (38%) $48a'' \rightarrow 52a''$ (31%) $48a'' \rightarrow 51a''$ (9%) $48a'' \rightarrow 50a''$ (8%) $46a'' \rightarrow 49a''$ (8%)	π–π*
$S_9(^1A')$	45944	0.00164	$48a'' \rightarrow 52a''$ (42%) $44a'' \rightarrow 49a''$ (35%) $46a'' \rightarrow 50a''$ (10%)	π–π*
$S_{10}(^1A'')$	47054	0.00175	$47a' \rightarrow 52a''$ (53%) $47a' \rightarrow 50a''$ (25%) $47a' \rightarrow 51a''$ (15%)	$n - \pi^*$

Table 2 Results of LR-TDDFT calculations for the ten lowest-lying excited singlet states of *cis*-4-styrylpyridine: excitation energy E (cm^{-1}), oscillator strength f and assignment; (the calculations were performed on the optimised B3LYP/$\mathscr{G}'$ geometry)

	E	f	Major MO → MO transitions	Main character
$S_1(^1A)$	32768	0.27822	$48a \rightarrow 49a$ (87%) $47a \rightarrow 49a$ (10%)	π–π*
$S_2(^1A)$	34016	0.06879	$47a \rightarrow 49a$ (84%) $48a \rightarrow 49a$ (10%)	*n*–π*
$S_3(^1A)$	36840	0.01750	$46a \rightarrow 49a$ (72%) $48a \rightarrow 50a$ (24%)	CT
$S_4(^1A)$	38587	0.00964	$45a \rightarrow 49a$ (76%) $48a \rightarrow 52a$ (14%)	CT
$S_5(^1A)$	40469	0.02349	$47a \rightarrow 50a$ (53%) $47a \rightarrow 52a$ (22%) $48a \rightarrow 50a$ (14%)	*n*–π*
$S_6(^1A)$	41202	0.03783	$48a \rightarrow 50a$ (35%) $44a \rightarrow 49a$ (17%) $47a \rightarrow 50a$ (14%) $46a \rightarrow 49a$ (12%) $48a \rightarrow 51a$ (9%)	π–π*
$S_7(^1A)$	41862	0.13867	$44a \rightarrow 49a$ (34%) $48a \rightarrow 51a$ (33%) $48a \rightarrow 50a$ (16%) $46a \rightarrow 49a$ (8%)	π–π*
$S_8(^1A)$	43626	0.00382	$48a \rightarrow 52a$ (59%) $45a \rightarrow 49a$ (16%) $46a \rightarrow 51a$ (10%) $48a \rightarrow 51a$ (7%)	π–π*
$S_9(^1A)$	45263	0.07866	$48a \rightarrow 51a$ (30%) $44a \rightarrow 49a$ (30%) $47a \rightarrow 51a$ (12%) $48a \rightarrow 52a$ (9%) $45a \rightarrow 50a$ (6%)	π–π*
$S_{10}(^1A)$	46263	0.05819	$47a \rightarrow 51a$ (70%) $44a \rightarrow 49a$ (7%) $47a \rightarrow 52a$ (7%) $48a \rightarrow 51a$ (5%)	π–π*

at 31794 cm^{-1}, which has a very strong oscillator strength. This transition involves the promotion of one electron from the bonding highest-occupied MO (HOMO) into the antibonding lowest-unoccupied MO (LUMO), which both are π orbitals delocalised over the entire molecule. The intense absorption band due to this π–π* transition masks the

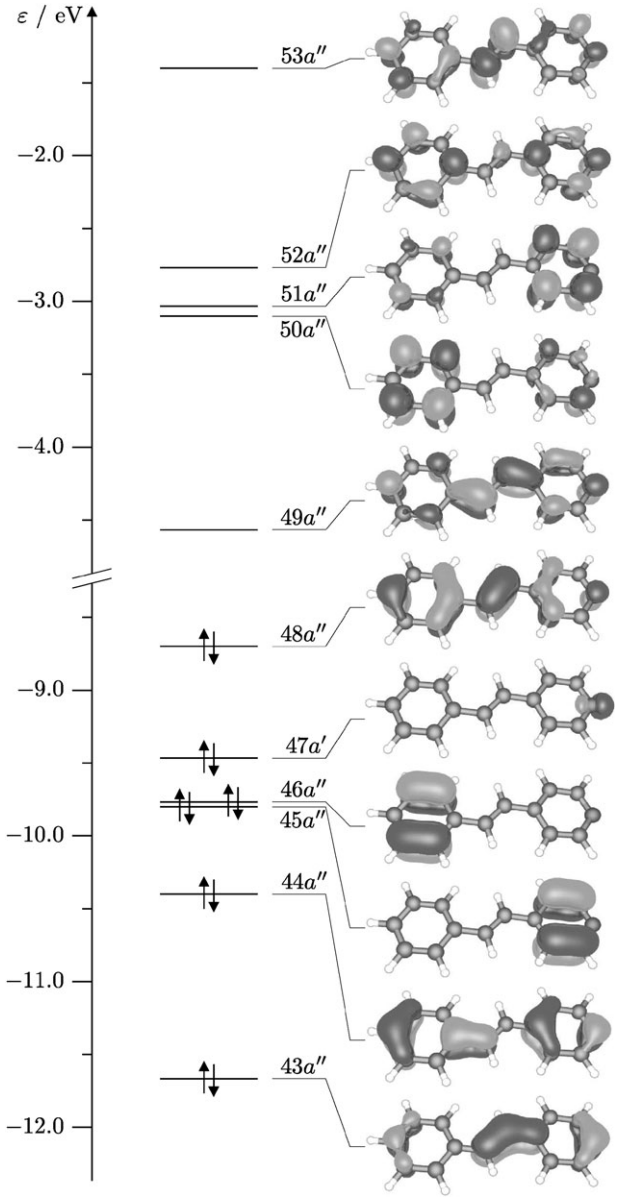

Fig. 2 Frontier KS MOs of *trans*-4-styrylpyridine: results of calculations performed at the B3LYP(AC)/$\mathscr{G}'$ level on the optimised B3LYP/$\mathscr{G}'$ geometry.

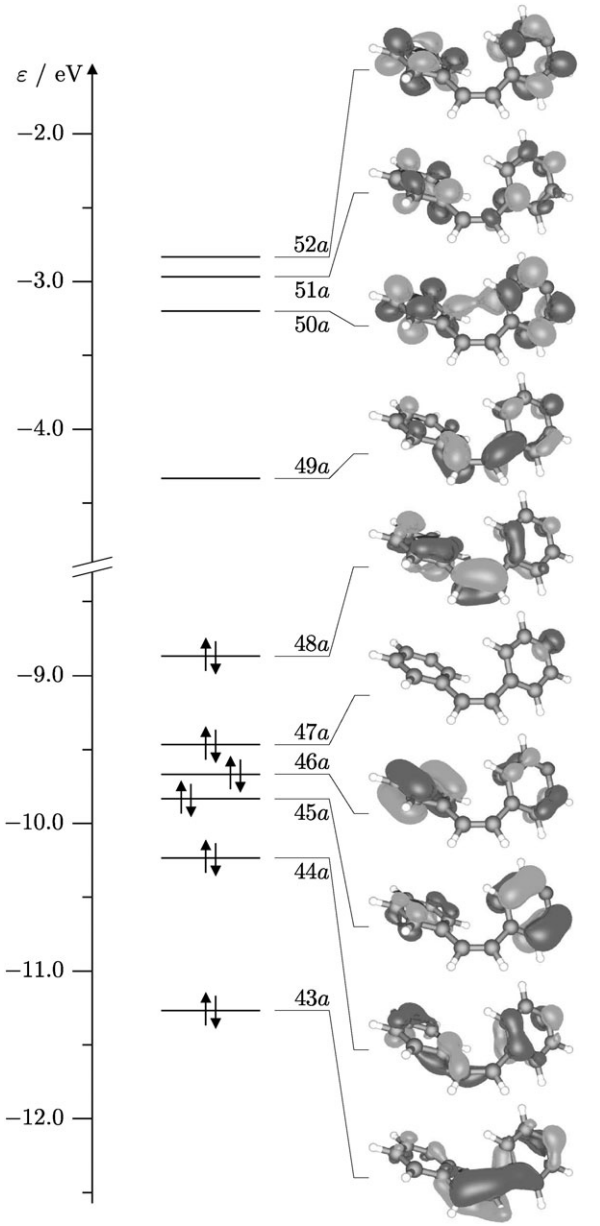

Fig. 3 Frontier KS MOs of *cis*-4-styrylpyridine: results of calculations performed at the B3LYP(AC)/$\mathscr{G}'$ level on the calculated B3LYP/$\mathscr{G}'$ geometry.

contributions of the $S_0 \rightarrow S_{2-4}$ transitions whose intensities are comparatively very weak. The S_1 and S_2 states are found to be nearly degenerate. The $S_0 \rightarrow S_2$ transition is an *n*–π* transition. It indeed involves a monoelectronic excitation from the HOMO − 1 σ-type orbital which describes the lone pair of the nitrogen atom into the LUMO. The transitions toward the S_3 and S_4 states are charge transfer (CT) transitions since they principally consist of the HOMO − 2 → LUMO and HOMO − 3 → LUMO excitations, respectively, and that the HOMO − 2 and HOMO − 3 orbitals are centred on the phenyl and pyridinyl fragments, respectively. The $S_0 \rightarrow S_5$ transition is an *n*–π* transition with no intensity. Finally, the $S_0 \rightarrow S_{6-8}$ transitions are at the origin of the second absorption band of *trans*-4-styrylpyridine. The intensity of this band is principally due to the $S_0 \rightarrow S_{6,7}$ transitions which are CT transitions. The $S_0 \rightarrow S_{9,10}$ transitions, whose intensities are weaker by one order of magnitude, take place at higher energies and do not contribute to the spectrum in the considered energy range.

For the *cis* isomer, the low-energy absorption band is due to the $S_0 \rightarrow S_1$ transition, as in the case of the *trans* isomer, but also to the $S_0 \rightarrow S_2$ transition which carries significant intensity in the present case. On going from the *trans* isomer to the *cis* isomer, the $S_0 \rightarrow S_1$ and $S_0 \rightarrow S_2$ transitions keep their respective π–π* and *n*–π* characters since their main MO → MO contributions are the HOMO → LUMO and HOMO − 1 → LUMO excitations, respectively (see Fig. 3). However, for the *cis* isomer, these single excitations mix with each other, in contrast to the situation met with the

trans isomer wherein such a mixing is symmetry forbidden. One thus notes in Table 2 that the HOMO − 1 → LUMO (resp. HOMO → LUMO) excitation contributes up to 10% to the $S_0 \rightarrow S_1$ (resp. $S_0 \rightarrow S_2$) transition. This suggests that the *n*–π* transition in the *cis* isomer actually borrows its intensity from the close lying π–π* transition. The $S_0 \rightarrow S_{3,4}$ transitions at higher energies are of CT character and contribute to the region of the spectrum which is intermediate between the two intense absorption bands. The transitions towards the S_5 and S_6 states of *n*–π* and π–π* characters, respectively, significantly contribute to the high-energy absorption band, as does the $S_0 \rightarrow S_9$ transition of π–π* character, but the main contribution to this absorption band is given by the $S_0 \rightarrow S_7$ transition of π–π* type. The intensities of the $S_0 \rightarrow S_{5-7,9}$ transitions make negligible the contribution of the $S_0 \rightarrow S_8$ (π–π*)-type transition of much weaker intensity.

In summary, the results of the LR-TDDFT calculations performed on the optimised geometries of the *cis* and *trans* isomers of 4-styrylpyridine have allowed us to give a first detailed analysis of their absorption spectra.

3.2 Further insight into the optical properties of 4-styrylpyridine from an approach based on AIMD

The above static analysis of the absorption spectra of the two isomers shows that their main absorption bands result only from the $S_0 \rightarrow S_{1,2}$ electronic excitations of close energies. For the *trans* isomer, the broadening of the involved transitions was ascribed by Marconi *et al.*[6] to the stretching progression of the C_1–C_2 ethylenic moiety, and the blurring of the vibronic structure at elevated temperatures to the presence of *trans* species that exhibit twisting around the C_{Ph}–C_1 and C_2–C_{Py} bonds (see Fig. 1 for the atom labelling used). The vibronic origin of the broadening of the electronic transitions and the assignment of the vibronic progression are supported by our finding that the π–π* $S_0 \rightarrow S_1$ and *n*–π* $S_0 \rightarrow S_2$ excitations mainly involve one-electron transitions into the LUMO, which exhibits an antibonding character at the level of the C_1–C_2 fragment. That is, the equilibrium geometries of *trans*-4-styrylpyridine in the $S_{1,2}$ states are significantly displaced with respect to the one in the S_0 state along the C_1–C_2 stretching vibrational coordinate. Actually, as shown below, several vibrational modes are involved in the vibronic progression. Furthermore, the existence of the twisted *trans* species has been evidenced by the results of the finite-temperature CPMD simulations reported in ref. 20. For the *cis* isomer, the $S_0 \rightarrow S_{1,2}$ electronic excitations also involve one-electron transitions into the LUMO, which still presents an antibonding character at the level of the C_1–C_2 ethylenic moiety. In addition, the results of the finite-temperature CPMD simulations performed on this isomer show that the aromatic rings also exhibit partial rotations about the C_{Ph}–C_1 and C_2–C_{Py} bonds. Consequently, the broadening of the electronic transitions at the origin of the main absorption band of *cis*-4-styrylpyridine is also vibronic in nature and the blurring of the vibronic structure can be ascribed to the thermal fluctuations.

For both isomers, the convolution of the calculated oscillator strengths with Gaussians helped us mimic the broadening of the electronic transitions within the static approach. However, such a procedure presents in the actual case three major drawbacks. (i) In order to reproduce the room-temperature spectra of the two isomers in CH_3OH (Fig. 1), it proved necessary to use Gaussians with a quite large full width at half maximum (FWHM) of 5000 cm^{-1}. Compared to the experimental spectra, (ii) the resulting simulated spectra are significantly red-shifted and (iii) the profiles of the main absorption bands are far too symmetric. A rigorous treatment of the broadening mechanism requires that the analysis accounts for both nuclear quantum and thermal fluctuation effects (see for instance ref. 40). The inclusion of the quantum effects is beyond the purpose of the present study. Still, as far as we are concerned with the analysis of the room-temperature spectra, we can limit ourselves to (i) the inclusion of the thermal effects, and (ii) an *ad hoc* treatment of the vibrational broadening. Let us first consider the influence of the thermal fluctuations.

3.2.1 Thermal fluctuation effects. The inclusion of the thermal effects is achieved by making use of the CPMD simulations performed at 300 K[20] to calculate the finite-temperature $S_0 \rightarrow S_I$ ($I \geq 1$) absorption lineshape $F_I(\nu)$ according to[41–43]

$$F_I(\nu) = \frac{1}{\Theta}\int_{\Theta} dt f_I(t)\delta(\nu_I(t) - \nu) = \frac{1}{N_R}\sum_{R=1}^{N_R} f_I^R \delta(\nu_I^R - \nu). \quad (1)$$

That is, for a simulation of total duration Θ, $F_I(\nu)$ is calculated as the average over N_R sample configurations from the values ν_I^R and f_I^R determined for the electronic transition energy $\nu_I(t)$ and the oscillator strength $f_I(t)$ for the considered configurations $R(t)$. The total absorption spectra is given by the sum

$$f(\nu) = \sum_{I=1}^{N_I} F_I(\nu). \quad (2)$$

For both isomers, $\Theta \approx 2.4$ ps.[20] For the calculations of the finite-temperature spectra, the recorded trajectories were sampled every $\Delta t \approx 95$ fs, for a total of $N_R = 26$ configurations. The electronic excitation calculations were performed at the B3LYP(AC)/$\mathscr{G}'$ level. We used in place of the δ functions Gaussians having a FWHM of 1500 cm^{-1},[45] and eqn (2) was evaluated using the $N_I = 10$ lowest-lying transitions which suffice for a complete characterisation of the main absorption band.[46]

The calculated 300 K and experimental spectra of the two isomers are shown in Fig. 4. Its inspection shows that, as compared to the results obtained within the static approach (Fig. 1), there is for both isomers a noticeable improvement in the relative positions of the calculated and experimental main absorption bands. One also notes that the asymmetry of these calculated bands bring them in better agreement with the experimental ones. Despite the improvement thus achieved by taking the thermal fluctuations into account, one notes for both isomers that the calculated main absorption bands are about two times narrower and about three times more intense than their experimental counterparts. This discrepancy can be ascribed to the neglect in our simulations of nuclear quantum effects. Indeed, the classical treatment of the nuclei leads to

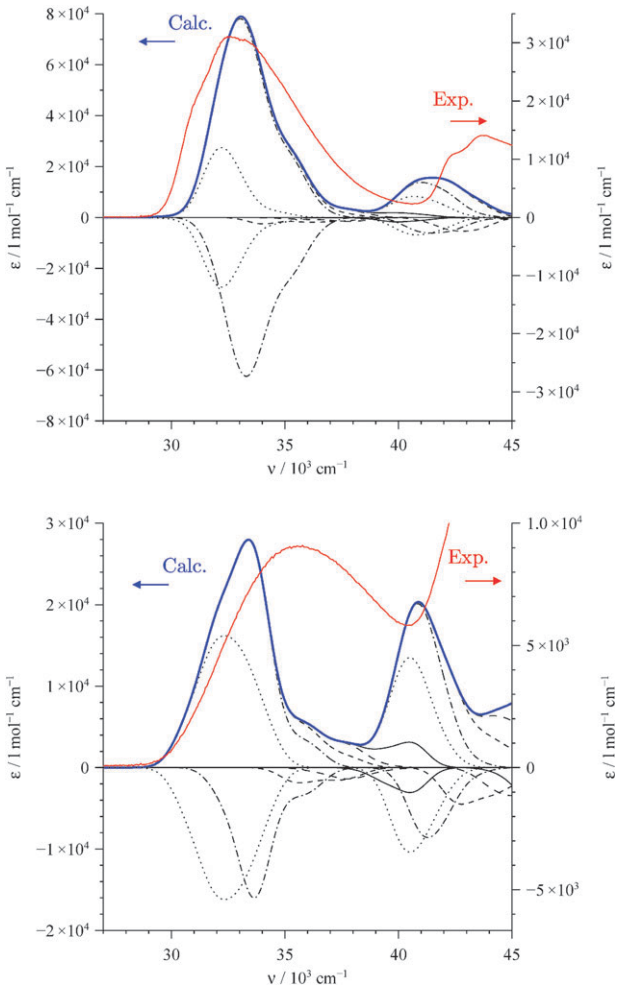

Fig. 4 Calculated 300 K (blue line, left *y*-axis) and experimental room-temperature (red line, right *y*-axis) absorption spectra of the *trans* (top) and *cis* (bottom) isomers of 4-styrylpyridine. The thin lines in the positive half of each plot are the composite partial spectra obtained from summing the $S_0 \rightarrow S_I$ ($I = 1,\ldots,10$) absorption bands, which are shown in the negative half of the plot.

absorption bands which are too narrow, because the thermal distribution of the "classical" nuclei is too narrow.[47] The lack of nuclear quantum effects can be compensated for by performing the simulations at higher temperatures (see ref. 47 and references therein). This discrepancy will be addressed later by determining the contributions of the relevant vibrational modes.

The fact remains nonetheless that the results of the actual calculations clearly show that the $S_0 \rightarrow S_1$ and $S_0 \rightarrow S_2$ transitions both contribute significantly to the finite-temperature main absorption bands of the two isomers. In the low-temperature limit ($T \rightarrow 0$ K), the same conclusion was drawn for the *cis* isomer from the results of the excitation calculations performed on its optimised geometry (Table 2). For the *trans* isomer however, the results of the excitation calculations similarly performed indicate that the main band is exclusively due to the $S_0 \rightarrow S_1$ transition of π–π* character, the close-lying *n*–π* $S_0 \rightarrow S_2$ transition having a comparatively vanishing intensity (Table 1).

At finite temperatures, the analysis of the main bands is not that simple. Fig. 5 shows the time dependence of the frontier KS levels of *trans*-4-styrylpyridine during the 300 K CPMD simulation. It also shows the occupied and virtual MOs which contribute to the $S_0 \rightarrow S_{1,2}$ transitions of the isomer at the selected simulation times of $t_0 = 0$ ps, $t_1 \approx 0.474$ ps, $t_2 = 1.517$ ps and $t_3 \approx 1.991$ ps. At $t = t_0$, the $S_0 \rightarrow S_1$ transition is found to occur at $E_1^{t_0} = 32174\,\mathrm{cm}^{-1}$ with an oscillatory strength $f_1^{t_0} = 0.96320$. The HOMO → LUMO excitation contributes 88% to this transition, which can therefore be identified as a π–π* transition. The $S_0 \rightarrow S_2$ transition is characterised by $E_2^{t_0} = 33459\,\mathrm{cm}^{-1}$ and $f_2^{t_0} = 0.03186$. It proves to be a π–π* CT transition as it is mainly contributed by the HOMO − 1 → LUMO and HOMO → LUMO + 1 excitations with weights of 72% and 16%, respectively. At t_1, the $S_0 \rightarrow S_{1,2}$ transitions have energies of $E_1^{t_1} = 32709\,\mathrm{cm}^{-1}$ and $E_2^{t_1} = 33298\,\mathrm{cm}^{-1}$, and oscillatory strengths of $f_1^{t_1} = 0.79829$ and $f_2^{t_1} = 0.27880$. The HOMO → LUMO and HOMO − 2 → LUMO excitations contribute 76% and 18%, respectively, to the $S_0 \rightarrow S_1$ transition, which thus has a π–π* character. The $S_0 \rightarrow S_2$ transition has an *n*–π* character: it indeed involves the HOMO − 2 → LUMO, HOMO − 1 → LUMO and HOMO → LUMO excitations, with respective contributions of 50%, 25% and 22%. As previously pointed out, within the C_s symmetry of the equilibrium geometry of the *trans* isomer, the π–π* and *n*–π* one-electron excitations are of distinct symmetries (*a*′ and *a*″, resp.), and their coupling is therefore symmetry forbidden. In the twisted *trans* forms of C_1 symmetry brought about by the thermal fluctuations, these symmetry restraints are lifted and the one-electron *n*–π* and π–π* excitations can couple. Thus, as observed for the $S_0 \rightarrow S_2$ transition at t_1, this allows that $S_0 \rightarrow S_I$ ($I \geq 1$) transitions of mainly *n*–π* character have noticeable intensities.

Actually, for most sample configurations (21 out of $N_R = 26$), those at $t_2 = 1.517$ ps and $t_3 \approx 1.991$ ps included, the $S_0 \rightarrow S_1$ and $S_0 \rightarrow S_2$ transitions are of *n*–π* and π–π* characters, respectively, and principally involve one-electron excitations from the HOMO − 1 and HOMO into the LUMO. In these cases, the $S_0 \rightarrow S_1$ transition is indeed mainly contributed by the HOMO − 1[*n*] → LUMO[π*] excitation and by the HOMO[π] → LUMO[π*] excitation to a lesser extent. Conversely, the $S_0 \rightarrow S_2$ transition originates mainly from the HOMO[π] → LUMO[π*] excitation and has a smaller contribution from the HOMO − 1[*n*] → LUMO[π*] excitation. The HOMO − 1, HOMO and LUMO are shown in Fig. 5 for the configurations at t_2 and t_3. At t_2, the HOMO − 1 → LUMO and HOMO → LUMO contribute 70% and 24%, respectively, to the $S_0 \rightarrow S_1$ transition ($E_1^{t_2} = 34822\,\mathrm{cm}^{-1}$, $f_1^{t_2} = 0.21954$), while they contribute 24% and 73%, respectively, to the $S_0 \rightarrow S_2$ transition ($E_2^{t_2} = 35395\,\mathrm{cm}^{-1}$, $f_2^{t_2} = 0.76897$). At t_3, the HOMO − 1 → LUMO and HOMO → LUMO contribute 86% and 9%, respectively, to the $S_0 \rightarrow S_1$ transition ($E_1^{t_3} = 31390\,\mathrm{cm}^{-1}$, $f_1^{t_3} = 0.07735$); and they contribute 9% and 89%, respectively, to the $S_0 \rightarrow S_2$ transition ($E_2^{t_3} = 32909\,\mathrm{cm}^{-1}$, $f_2^{t_3} = 1.09903$). As illustrated by these results obtained for the configurations at t_2 and t_3, the intensity of the $S_0 \rightarrow S_1$ transition tends to be stronger the larger the contribution of the HOMO → LUMO excitation.

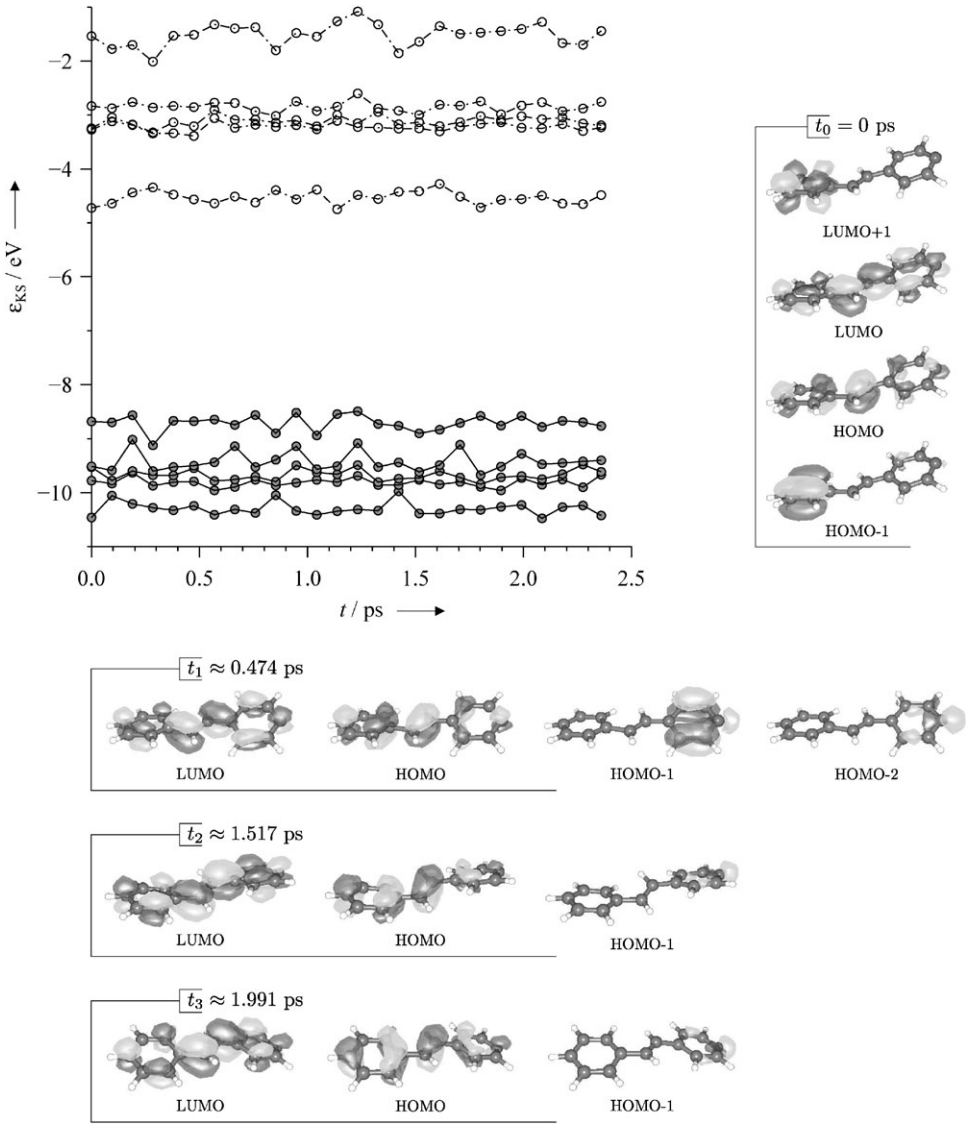

Fig. 5 Time dependence of the occupied (filled circles) and virtual (empty circles) frontier KS energy levels of *trans*-4-styrylpyridine as obtained at the B3LYP(AC)/$\mathscr{G}'$ level from the CPMD simulation performed at 300 K.[20] Molecular orbitals are also shown for some instantaneous configurations (see text).

However, the intensity of this transition remains weaker than that of the $S_0 \rightarrow S_2$ transition. The time-averaged oscillatory strengths of these transitions

$$\bar{f}_I = \frac{1}{\Theta}\int_{\Theta} \mathrm{d}t f_I(t) = \frac{1}{N_R}\sum_{R=1}^{N_R} f_I^R \qquad (3)$$

are $\bar{f}_1 = 0.26487$ and $\bar{f}_2 = 0.77443$; that is, $\bar{f}_1 < \bar{f}_2$ as expected.

The time evolution of the frontier KS levels of the *cis* isomer obtained from the 300 K CPMD simulation is shown in Fig. 6, along with occupied and virtual MOs involved in the $S_0 \rightarrow S_{1,2}$ transitions at $t'_0 = 0$ ps, $t'_1 \approx 0.578$ ps, $t'_2 \approx 1.612$ ps and $t'_3 \approx 1.991$ ps. At t'_0, the $S_0 \rightarrow S_1$ transition ($E_1^{t'_0} = 32929\,\mathrm{cm}^{-1}$, $f_1^{t'_0} = 0.72934$) is a π–π* transition, with a dominant 93% contribution from the HOMO → LUMO excitation. The $S_0 \rightarrow S_2$ transition of weaker intensity ($E_2^{t'_0} = 34395\,\mathrm{cm}^{-1}$, $f_2^{t'_0} = 0.04808$) has an *n*–π* character as it mainly involve that the HOMO − 3 → LUMO and HOMO → LUMO one-electron excitations with 65% and 23% contributions, respectively. At t'_1, the $S_0 \rightarrow S_1$ transition ($E_1^{t'_1} = 31530\,\mathrm{cm}^{-1}$, $f_1^{t'_1} = 0.06582$) has an *n*–π* character given that the HOMO − 1 → LUMO and HOMO → LUMO excitations contribute 66% and 33%, respectively, to this transition. As for the $S_0 \rightarrow S_2$ transition ($E_2^{t'_1} = 33518\,\mathrm{cm}^{-1}$, $f_2^{t'_1} = 0.32469$), the HOMO → LUMO and HOMO − 1 → LUMO contribute by 62% and by 29% respectively, to this transition which has therefore a π–π* character. However, for most sample configurations (19 out of $N_R = 26$), the $S_0 \rightarrow S_1$ and $S_0 \rightarrow S_2$ transitions are of π–π* and *n*–π* characters, respectively, and are essentially contributed by excitations from the HOMO − 1 and HOMO into the LUMO. In these

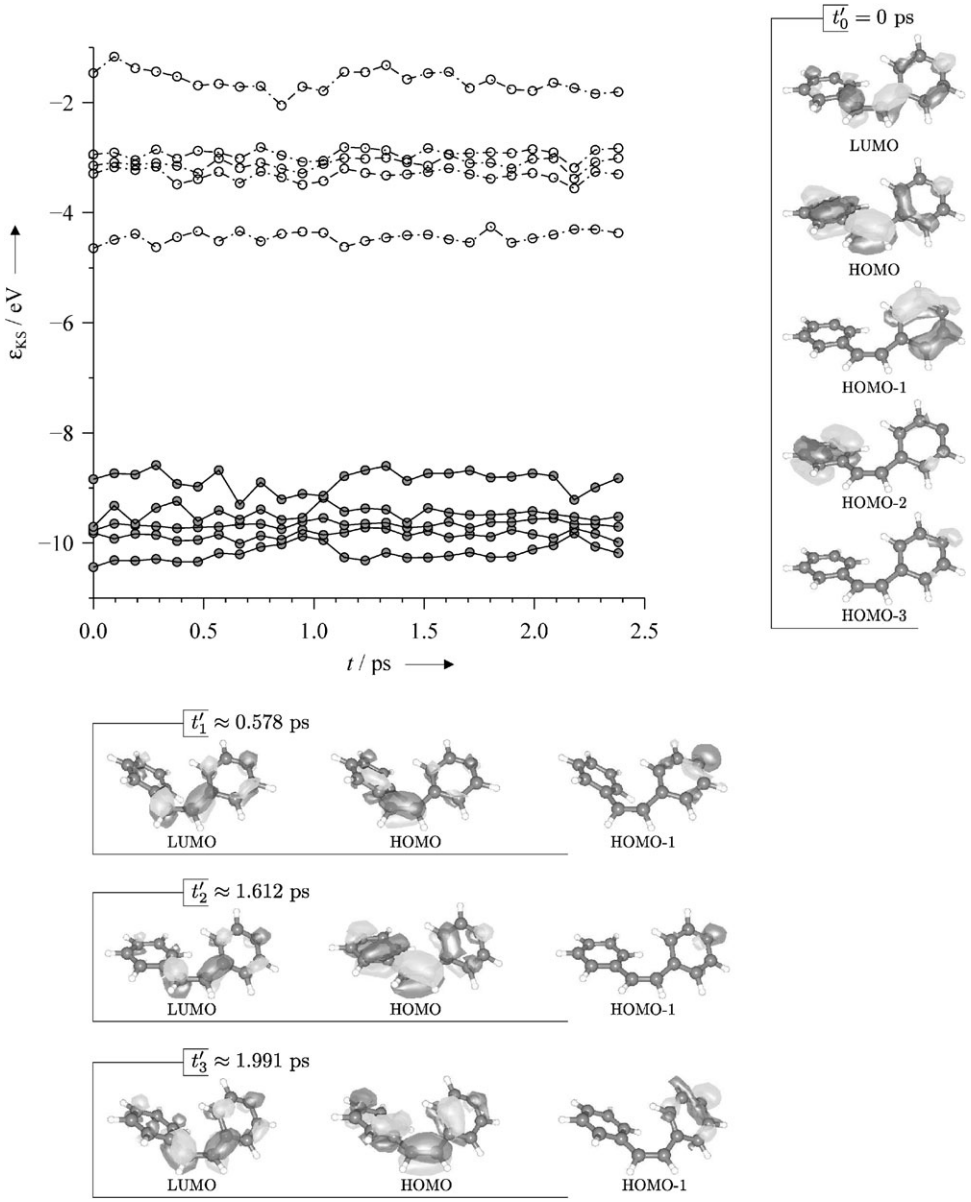

Fig. 6 Time dependence of the occupied (filled circles) and virtual (empty circles) frontier KS energy levels of *cis*-4-styrylpyridine as obtained at the B3LYP(AC)/$\mathscr{G}'$ level from the CPMD simulation performed at 300 K.[20] Molecular orbitals are also shown for some instantaneous configurations (see text).

configurations, those at t'_2 and t'_3 included, the $S_0 \rightarrow S_1$ is mainly contributed by the HOMO[π] → LUMO[π*] excitation with a smaller contribution from the HOMO − 1[*n*] → LUMO[π*] excitation. On the other hand, the $S_0 \rightarrow S_2$ transition originates mainly from the HOMO − 1[*n*] → LUMO[π*] excitation and the HOMO[π] → LUMO[π*] excitation has a smaller contribution. At t'_2, the contributions of the HOMO → LUMO and HOMO − 1 → LUMO excitations to the $S_0 \rightarrow S_1$ transition ($E_1^{t'_2} = 31761\,\mathrm{cm}^{-1}$, $f_1^{t'_2} = 0.22341$) are 63% and 35%, respectively. They become 58% and 33% for the $S_0 \rightarrow S_2$ transition ($E_2^{t'_2} = 33290\,\mathrm{cm}^{-1}$, $f_2^{t'_2} = 0.26215$). At t'_3, the HOMO → LUMO excitation contributes 91% to the $S_0 \rightarrow S_1$ transition ($E_1^{t'_2} = 31378\,\mathrm{cm}^{-1}$, $f_1^{t'_2} = 0.22760$), whereas the HOMO − 1 → LUMO contributes 90% the $S_0 \rightarrow S_2$ transition ($E_2^{t'_2} = 32888\,\mathrm{cm}^{-1}$, $f_2^{t'_2} = 0.01750$). As shown with these results at t'_2 and t'_3, the instantaneous π–π* $S_0 \rightarrow S_1$ transition is not necessary more intense than the *n*–π* $S_0 \rightarrow S_2$ transition, although this proves to occur quite often (12 out of the considered 19 configurations). Note that the time-averaged oscillatory strengths (eqn (3)) of the $S_0 \rightarrow S_1$ and $S_0 \rightarrow S_2$ transitions are $\bar{f}'_1 = 0.22943$ and $\bar{f}'_2 = 0.16936$, in agreement with the fact that the former tends to be more intense than the latter. Finally, the overall intensity of the main absorption band dominated by the $S_0 \rightarrow S_{1,2}$ transitions is $\bar{f}'_1 + \bar{f}'_2 = 0.39879$. For the *trans* isomer, the overall intensity of the main absorption band is $\bar{f}'_1 + \bar{f}'_2 = 1.03930$, that is, about 2.6 stronger than that of the *cis* isomer, in agreement with experiment.

3.2.2 Vibronic broadening. The calculation of the absorption spectra as time averages over CPMD trajectories helped evidence the major role played by the thermal fluctuations in the finite-temperature absorption spectra of the flexible 4-styrylpyridine molecule in its *cis* and *trans* forms. However, except for the vibrations whose frequencies are below the thermal energy k_BT, the vibrational contributions to the absorption bands cannot be captured by this approach wherein the nuclei are treated classically. In order to remedy this deficiency, the missing contributions can be determined in an *ad hoc* manner. Thus, in their classical molecular dynamics study of the influence of thermal motions on the structure and absorption spectra of stilbene and models of poly(*p*-phenylenevinylene), Kwasniewski *et al.*[48] addressed this issue by associating a vibronic progression to the electronic transition determined for each of the sample configurations. They used one effective mode and could this way account for the cumulated effect of thermal and vibronic broadenings. We have proceeded similarly but, instead of using effective modes, we have evaluated for both isomers the contributions of their vibrational modes which are not thermally excited. That is, given that $k_BT \approx 200\ \mathrm{cm}^{-1}$, we have considered the modes with frequencies $\nu_k \geq 200\ \mathrm{cm}^{-1}$ and calculated their contributions within the displaced harmonic oscillator approximation, assuming that their ground vibrational levels only are populated. In this framework, the vibrational intensity distribution $F_I^{v}(\nu)$ associated with the electronic transition $S_0 \rightarrow S_I$ of energy ν_I and oscillator strength f_I reads

$$F_I^{v}(v) = f_I \sum_{n_1} \cdots \sum_{n_p} \left(\prod_{k=1}^{p} \mathscr{F}_{I,k}(0, n_k) \right) \times \delta \left[v - v_I - \sum_{k=1}^{p} n_k v_k \right]. \quad (4)$$

In the above equation, p is the number of considered vibrations; n_k denotes the vibrational state reached in the S_I state for the k-th vibration of frequency ν_k; and $\mathscr{F}_{I,k}(n'_k,n_k)$ is the associated Franck–Condon factor, that is, the squared overlap integral between the vibrational wavefunction $|\chi_{0,k,n'_k}\rangle$ of the k-th mode in the ground state (here, $n'_k = 0$) and the vibrational wavefunction $|\chi_{I,k,n_k}\rangle$ of this mode in the excited state. Within the displaced harmonic oscillator approximation, the Franck–Condon factors $\mathscr{F}_{I,k}(0,n_k)$ read[49,50]

$$\mathscr{F}_{I,k}(0, n_k) = \frac{(\mathscr{S}_{I,k})^{n_k}}{n_k!} \times \exp(-\mathscr{S}_{I,k}), \quad (5)$$

where $\mathscr{S}_{I,k}$ is the dimensionless Huang–Rhys factor[51] for the k-th mode in the S_I state, given by

$$\mathscr{S}_{I,k} = \frac{1}{2} \frac{\omega_k}{\hbar} (Q_{I,k})^2. \quad (6)$$

ω_k is the angular frequency, and $Q_{I,k}$ is the displacement induced along the k-th normal mode by the $S_0 \rightarrow S_I$ change of states. $Q_{I,k}$ is given by the projection of the mass-weighted S_I/S_0 geometric changes onto the normalised eigenvector of the k-th mass-weighted normal mode (see, for instance, ref. 52 and 53). Hence, its calculation and consequently that of the Franck–Condon factors necessitate the determination of the relaxed S_0 and S_I geometries, as well as the characterisation of the ground-state vibrational properties.

For our purposes, the vibrational properties of the *cis* and *trans* isomers of 4-styrylpyridine have been characterised at the B3LYP/$\mathscr{G}$ level. Given that we are interested in the analysis of their main absorption bands which originate from the $S_0 \rightarrow S_1$,S_2 transitions, attempts were made to determine their S_1 and S_2 optimised geometries at this same level. They proved to be conclusive only for the calculations targeted at the determination of the S_1 structures. At these stationary points found at the B3LYP/$\mathscr{G}$ for the two isomers, the S_1 state has a π–π^* character. No stationary point could be found for the *trans* isomer in the S_2 state because of the proximity of the S_1 and S_2 potential energy surfaces in the probed region, which actually is the vicinity of the S_1 stationary point. We indeed observed during the dedicated optimisation calculations that the character of the second excited state alternates between π–π^* and n–π^*, and that the energies of these two states remain above the energy of the S_1 stationary point by 3 mHa at most. This suggests that the relaxed geometries of the *trans* isomer in the S_1 and S_2 states are very similar. We consequently used the S_1 relaxed geometry for the calculation of the $S_0 \rightarrow S_2$ Huang–Rhys factors. As shown below, this led to very satisfactory results.

In the case of the *cis* isomer, the B3LYP/$\mathscr{G}$ relaxed S_1 structure turned out to be nonphysically distorted with H atoms pertaining to the phenyl and pyridinyl groups that markedly lie out of the planes defined by the aromatic cycles (see the ESI†). Furthermore the use of this structure for the computation of the vibronic contributions to the main absorption band of the *cis* isomer led to a predicted band which is three orders of magnitude weaker than observed (the calculated Huang–Rhys factors are given in the ESI†). The fact that the calculated B3LYP/$\mathscr{G}$ geometry of the *cis* isomer in the S_1 state is so severely distorted suggests that the use of the B3LYP functional leads to an overestimation of the van der Waals interactions, which is responsible for the aromatic rings coming too close to each other. Indeed, increasing the quality of the basis set used with the B3LYP functional did not led to an improved geometry (data not shown), while the use of an other functional, namely the BOP functional, in combination with the $\mathscr{G}$ basis set gave a S_1 structure, which is physically more sound, and which also led to a predicted main absorption band in pretty good agreement with experiment (see below). The assessment of the functionals for predicting the excited-state structure of the twisted *cis*-4-styrylpyridine would deserve a whole study. Here, we limited ourselves to the determination at the BOP/$\mathscr{G}$ level of the vibrational properties of the *cis* isomer and of its structure in the S_1 state. Its structure in the S_2 state could also be determined. At the stationary points found for the *cis* isomer in the S_1 and S_2 states, these states have n–π^* and π–π^* character, respectively. Selected distances and angles characterising the structures determined for the two isomers in the ground and excited states are summarised in Table 3. The values found for these structural parameters in the previously reported B3LYP/$\mathscr{G}$ S_0 geometries[20] are also given for comparison.

Table 3 Selected distances (Å) and angles (deg) in optimised *trans* and *cis* geometries of 4-styrylpyridine

	C_{Ph}–C_1	C_1–C_2	C_2–C_{Py}	C_{Ph}–C_1–C_2	C_1–C_2–C_{Py}	τ^a	$\angle$(Py,Ph)^b
trans-4-Styrylpyridine in the S_0 ground state							
B3LYP/$\mathscr{G}'^c$	1.468	1.351	1.468	127.3	126.4	180.0	0.0
B3LYP/$\mathscr{G}$	1.469	1.354	1.469	127.3	126.1	180.0	0.0
trans-4-Styrylpyridine in the S_1 state							
B3LYP/$\mathscr{G}^d$	1.420	1.422	1.421	124.7	124.9	180.0	0.0
cis-4-Styrylpyridine in the S_0 ground state							
B3LYP/$\mathscr{G}'^c$	1.473	1.345	1.472	130.8	130.5	6.4	52.3
B3LYP/$\mathscr{G}$	1.478	1.356	1.479	130.9	130.6	7.7	50.5
BOP/$\mathscr{G}$	1.486	1.371	1.485	132.1	131.9	8.2	49.9
cis-4-Styrylpyridine in the S_1 state							
B3LYP/$\mathscr{G}^d$	1.418	1.414	1.414	122.9	122.5	20.1	24.2
BOP/$\mathscr{G}^e$	1.443	1.426	1.443	131.9	130.0	30.1	48.3
cis-4-Styrylpyridine in the S_2 state							
BOP/$\mathscr{G}^d$	1.439	1.433	1.433	127.1	126.0	32.7	43.5

[a] τ = C_{Ph}–C_1–C_2–C_{Py}. [b] $\angle$(Py,Ph) is the angle between planes defined by the phenyl and pyridinyl cycles. [c] Taken from ref. 20. [d] At this stationary point, the considered state has a π–π* character. [e] At this stationary point, the considered state has an *n*–π* character.

For 4-styrylpyridine in the ground state, inspection of Table 3 shows that there is, for its two isomers, a good agreement between the previously reported geometries and the actual ones. One also notes for the *trans* isomer that the $S_0 \rightarrow S_1$ change of states translates into a ≈0.07 Å increase of the C_1–C_2 bond length and a ≈0.05 Å decrease of the C_{Ph}–C_1 and C_2–C_{Py} bond lengths. The resulting loss of the bond length alternation in the C_{Ph}–C_1–C_2–C_{Py} unit is accompanied by a decrease of 2.6 deg and 1.2 deg of the angles C_{Ph}–C_1–C_2 and C_1–C_2–C_{Py}, respectively, and is in fact similar to the one found for the parent *trans*-stilbene upon the $S_0 \rightarrow S_1$ change of states.[54,55] When one considers the results obtained at the BOP/$\mathscr{G}$ level for the *cis* isomer, one also notes that there is the same loss of bond length alternation upon the $S_0 \rightarrow S_1$ and $S_0 \rightarrow S_2$ changes of states: it results in both cases from a lengthening of ≈0.06 Å of the C_1–C_2 bond and a shortening of ≈0.05 Å of the C_{Ph}–C_1 and C_2–C_{Py} bonds. The most noticeable differences between the BOP/$\mathscr{G}$ S_1 and S_2 geometries proves to be in the values of the selected angles, that is, in the spatial arrangement of the phenyl and pyridinyl substituents. Thus, upon the $S_0 \rightarrow S_1$ change of states: the angles C_{Ph}–C_1–C_2 and C_1–C_2–C_{Py} decrease by 0.3 and 1.9 deg, the torsion angle τ = C_{Ph}–C_1–C_2–C_{Py} increases by 21.9 deg, and the angle $\angle$(Py,Ph) between the two aromatic rings decreases by 1.6 deg. These changes are actually more pronounced for the $S_0 \rightarrow S_2$ change of states: indeed, the angles C_{Ph}–C_1–C_2 and C_1–C_2–C_{Py} decrease by 5.0 and 5.9 deg, τ increases by 24.5 deg, and $\angle$(Py,Ph) decreases by 5.4 deg. Note that the B3LYP/$\mathscr{G}$ bond lengths reported in Table 3 for the *cis* isomer also supports the loss of bond alternation upon excitation. However, because of the unphysical stacking of the phenyl and pyridinyl substituents mentioned above, the B3LYP/$\mathscr{G}$ values of the selected angles in the excited-state *cis* geometry drastically differ from those obtained at the BOP/$\mathscr{G}$ level, whether one considers the BOP/$\mathscr{G}$ S_1 or S_2 geometry.

Tables 4 and 5 show the coordinates and frequencies of selected vibration modes of the *cis* and *trans* isomers, respectively. For the two isomers, the selected modes are those with frequencies greater than 200 cm^{-1} and with the largest $S_0 \rightarrow S_1$ and/or $S_0 \rightarrow S_2$ Huang–Rhys factors (*i.e.*, with $\mathscr{S}_I$ values (I = 1, 2) greater than the arbitrary threshold of 0.04). Note that, in the case of the *trans* isomer, the Huang–Rhys factors are likely to be non-vanishing only for the totally symmetric a' modes because of the C_s molecular symmetry of the ground-state and excited-state geometries. For both isomers, the selected modes include the stretching of the C_1–C_2 ethylenic moiety which, in both cases, is the mode of index 58. This naturally follows from the fact that the electronic transitions of interest correspond to one-electron transitions into the LUMO, which exhibits an antibonding character at the level of the C_1–C_2 fragment. However, as explained above, the structural changes induced by these transitions are not limited to the ethylenic moiety, whence the large number of Franck–Condon active modes.

There are 13 selected active modes for the *trans* isomer and 30 for the *cis* isomer (Tables 4 and 5). For the evaluation of the vibrational intensity distribution functions $F_I^v(\nu)$ (eqn (4)), even larger numbers of coupling vibrational modes were considered, namely, those with Huang–Rhys factors $\mathscr{S}_I \geq 0.001$ (I = 1, 2; see the ESI†). An in-house C++ program was used for this purpose. In order to reduce the computation cost tied to the evaluation of eqn (4), it is possible to only keep the products of the Franck–Condon factors which are above a given limit ε_{lim}. In the present case, we used for both isomers $\varepsilon_{lim} = 10^{-7}$ as this threshold warrants the convergence of the vibrational intensity distribution functions, and more especially the convergence of their high-energy tails of weak intensity. We also used Gaussian convolution functions.

Fig. 7 and 8 show the vibronic progressions determined for the two isomers using a vanishing value of the electronic transition energy, an oscillator strength of one, and Gaussians with FWHM of 400 cm^{-1} and 800 cm^{-1}. For the *trans* isomer (Fig. 7), the curves obtained are well structured and suggest that one could use an effective vibrational mode with an associated frequency of 1500–1600 cm^{-1}, which thus proves to be quite close to the frequency of the stretching of the ethylenic moiety. The value of the FWHM influences the heights of the peaks but the overall intensity given by the area under the curve is preserved. In the case of the *cis* isomer (Fig. 8), the calculated vibronic progressions are less structured. The $F_1^v(\nu)$ and $F_2^v(\nu)$ profiles thus obtained are quite comparable and correspond to broad bands which are centred

Table 4 *trans*-4-Styrylpyridine: coordinates and frequencies of the normal modes with frequencies greater than 200 cm^{-1}, and for which the largest $S_0 \rightarrow S_1$ Huang–Rhys factors $\mathscr{S}_1$ are found ($\mathscr{S}_1 \geq 0.04$; B3LYP/$\mathscr{G}$ results)

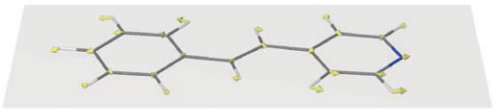

$\nu_5(a') = 202\ cm^{-1}$

$\mathcal{S}_1 = 0.853$

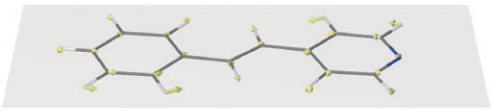

$\nu_7(a') = 284\ cm^{-1}$

$\mathcal{S}_1 = 0.055$

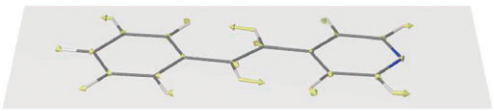

$\nu_{25}(a') = 883\ cm^{-1}$

$\mathcal{S}_1 = 0.052$

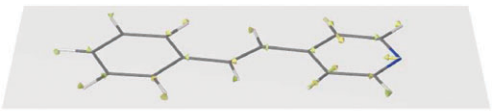

$\nu_{32}(a') = 1001\ cm^{-1}$

$\mathcal{S}_1 = 0.055$

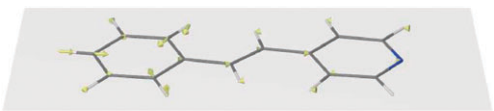

$\nu_{33}(a') = 1005\ cm^{-1}$

$\mathcal{S}_1 = 0.056$

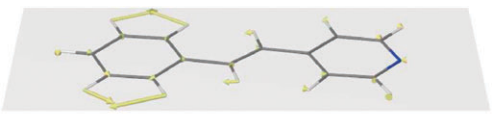

$\nu_{40}(a') = 1200\ cm^{-1}$

$\mathcal{S}_1 = 0.041$

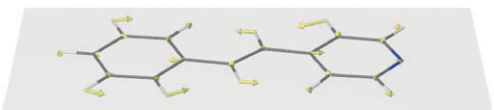

$\nu_{41}(a') = 1215\ cm^{-1}$

$\mathcal{S}_1 = 0.063$

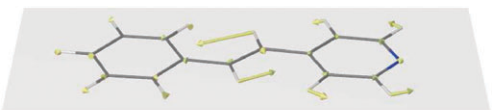

$\nu_{46}(a') = 1337\ cm^{-1}$

$\mathcal{S}_1 = 0.043$

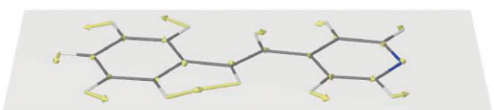

$\nu_{47}(a') = 1357\ cm^{-1}$

$\mathcal{S}_1 = 0.085$

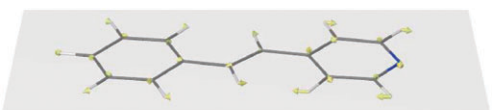

$\nu_{54}(a') = 1597\ cm^{-1}$

$\mathcal{S}_1 = 0.084$

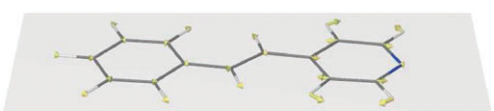

$\nu_{56}(a') = 1636\ cm^{-1}$

$\mathcal{S}_1 = 0.184$

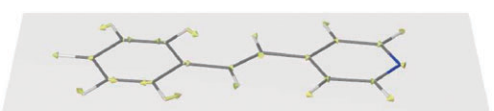

$\nu_{57}(a') = 1649\ cm^{-1}$

$\mathcal{S}_1 = 0.073$

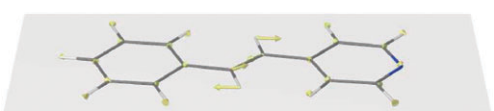

$\nu_{58}(a') = 1690\ cm^{-1}$

$\mathcal{S}_1 = 0.384$

Table 5 *cis*-4-styrylpyridine: coordinates and frequencies of the normal modes with frequencies greater than 200 cm^{-1}, and for which the largest $S_0 \rightarrow S_I$ Huang–Rhys factors $\mathscr{S}_I$ are found ($I = 1,2$; $\mathscr{S}_1 \geq 0.04$ or $\mathscr{S}_2 \geq 0.04$; BOP/$\mathscr{G}$ results)

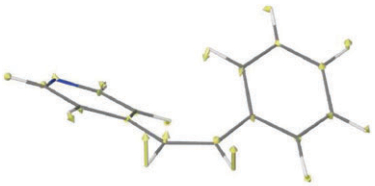

$\nu_6(a) = 237\ cm^{-1}$

$\mathcal{S}_1 = 0.048$ $\mathcal{S}_2 = 0.000$

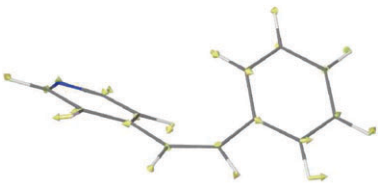

$\nu_7(a) = 259\ cm^{-1}$

$\mathcal{S}_1 = 0.083$ $\mathcal{S}_2 = 0.109$

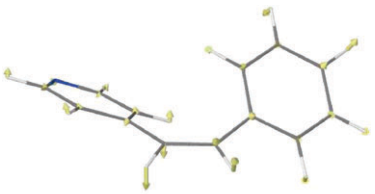

$\nu_9(a) = 389\ cm^{-1}$

$\mathcal{S}_1 = 0.914$ $\mathcal{S}_2 = 2.074$

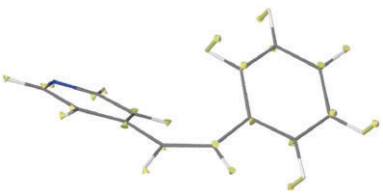

$\nu_{10}(a) = 399\ cm^{-1}$

$\mathcal{S}_1 = 0.030$ $\mathcal{S}_2 = 0.046$

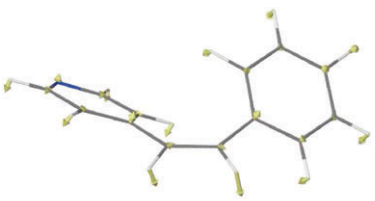

$\nu_{11}(a) = 451\ cm^{-1}$

$\mathcal{S}_1 = 0.001$ $\mathcal{S}_2 = 0.069$

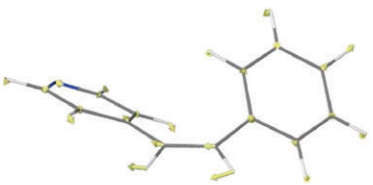

$\nu_{12}(a) = 495\ cm^{-1}$

$\mathcal{S}_1 = 0.494$ $\mathcal{S}_2 = 0.114$

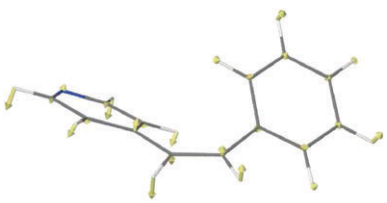

$\nu_{14}(a) = 564\ cm^{-1}$

$\mathcal{S}_1 = 0.396$ $\mathcal{S}_2 = 0.657$

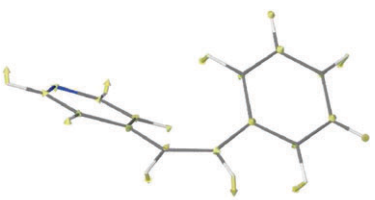

$\nu_{17}(a) = 680\ cm^{-1}$

$\mathcal{S}_1 = 0.055$ $\mathcal{S}_2 = 0.006$

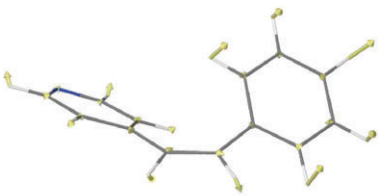

$\nu_{18}(a) = 691\ cm^{-1}$

$\mathcal{S}_1 = 0.047$ $\mathcal{S}_2 = 0.000$

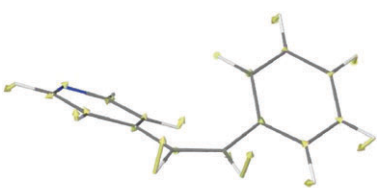

$\nu_{19}(a) = 722\ cm^{-1}$

$\mathcal{S}_1 = 0.057$ $\mathcal{S}_2 = 0.059$

Table 5 (*continued*)

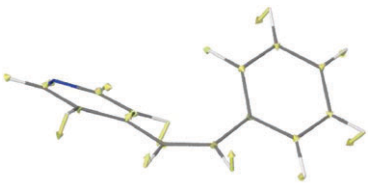

$\nu_{20}(a) = 734\ \mathrm{cm}^{-1}$

$\mathcal{S}_1 = 0.383$ $\mathcal{S}_2 = 0.136$

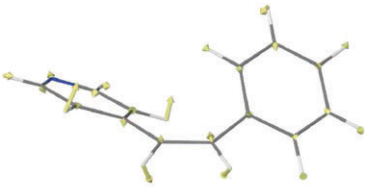

$\nu_{21}(a) = 747\ \mathrm{cm}^{-1}$

$\mathcal{S}_1 = 0.118$ $\mathcal{S}_2 = 0.000$

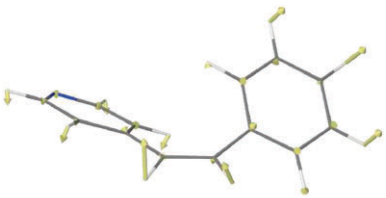

$\nu_{22}(a) = 772\ \mathrm{cm}^{-1}$

$\mathcal{S}_1 = 0.045$ $\mathcal{S}_2 = 0.074$

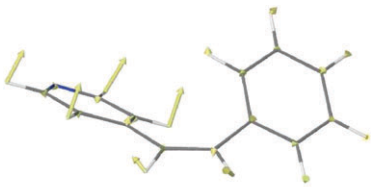

$\nu_{23}(a) = 811\ \mathrm{cm}^{-1}$

$\mathcal{S}_1 = 0.174$ $\mathcal{S}_2 = 0.087$

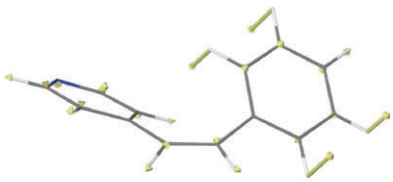

$\nu_{24}(a) = 834\ \mathrm{cm}^{-1}$

$\mathcal{S}_1 = 0.021$ $\mathcal{S}_2 = 0.045$

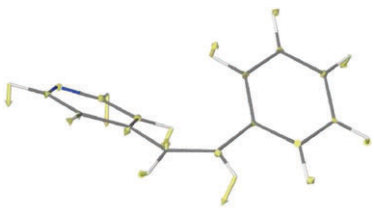

$\nu_{25}(a) = 860\ \mathrm{cm}^{-1}$

$\mathcal{S}_1 = 0.066$ $\mathcal{S}_2 = 0.002$

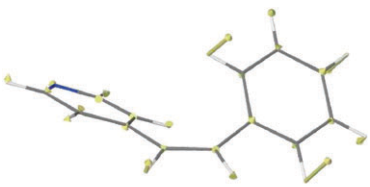

$\nu_{27}(a) = 908\ \mathrm{cm}^{-1}$

$\mathcal{S}_1 = 0.053$ $\mathcal{S}_2 = 0.096$

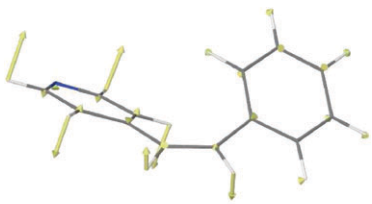

$\nu_{28}(a) = 938\ \mathrm{cm}^{-1}$

$\mathcal{S}_1 = 0.013$ $\mathcal{S}_2 = 0.149$

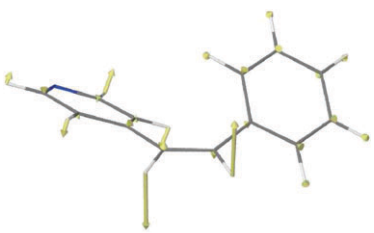

$\nu_{29}(a) = 946\ \mathrm{cm}^{-1}$

$\mathcal{S}_1 = 0.145$ $\mathcal{S}_2 = 0.306$

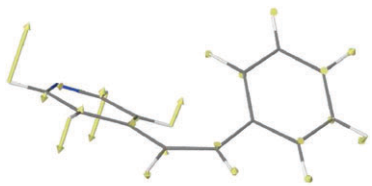

$\nu_{31}(a) = 955\ \mathrm{cm}^{-1}$

$\mathcal{S}_1 = 0.005$ $\mathcal{S}_2 = 0.096$

Table 5 (*continued*)

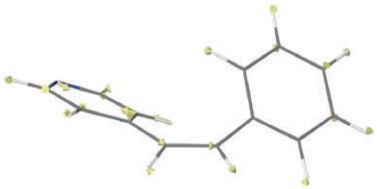

$\nu_{32}(a) = 962\ \mathrm{cm}^{-1}$

$\mathcal{S}_1 = 1.130$ $\mathcal{S}_2 = 0.053$

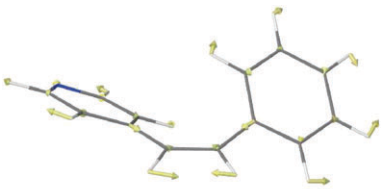

$\nu_{39}(a) = 1139\ \mathrm{cm}^{-1}$

$\mathcal{S}_1 = 0.286$ $\mathcal{S}_2 = 0.077$

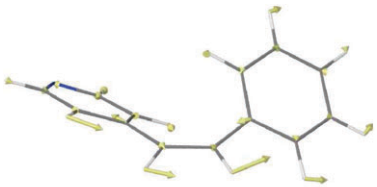

$\nu_{42}(a) = 1193\ \mathrm{cm}^{-1}$

$\mathcal{S}_1 = 0.101$ $\mathcal{S}_2 = 0.006$

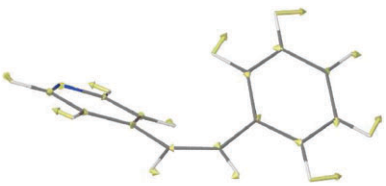

$\nu_{52}(a) = 1467\ \mathrm{cm}^{-1}$

$\mathcal{S}_1 = 0.011$ $\mathcal{S}_2 = 0.042$

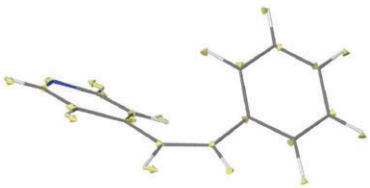

$\nu_{54}(a) = 1522\ \mathrm{cm}^{-1}$

$\mathcal{S}_1 = 0.029$ $\mathcal{S}_2 = 0.070$

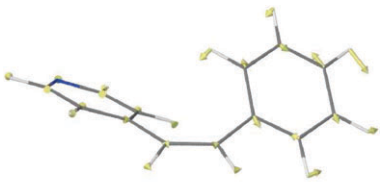

$\nu_{55}(a) = 1555\ \mathrm{cm}^{-1}$

$\mathcal{S}_1 = 0.010$ $\mathcal{S}_2 = 0.052$

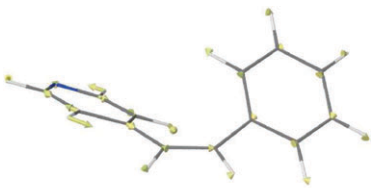

$\nu_{56}(a) = 1566\ \mathrm{cm}^{-1}$

$\mathcal{S}_1 = 0.002$ $\mathcal{S}_2 = 0.069$

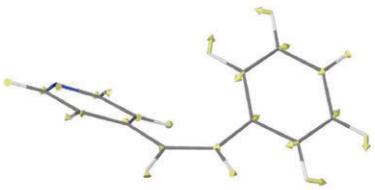

$\nu_{57}(a) = 1579\ \mathrm{cm}^{-1}$

$\mathcal{S}_1 = 0.074$ $\mathcal{S}_2 = 0.049$

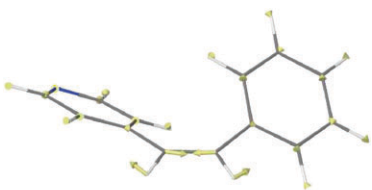

$\nu_{58}(a) = 1607\ \mathrm{cm}^{-1}$

$\mathcal{S}_1 = 0.129$ $\mathcal{S}_2 = 0.066$

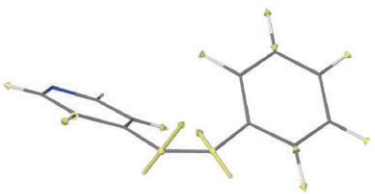

$\nu_{63}(a) = 3102\ \mathrm{cm}^{-1}$

$\mathcal{S}_1 = 0.016$ $\mathcal{S}_2 = 0.065$

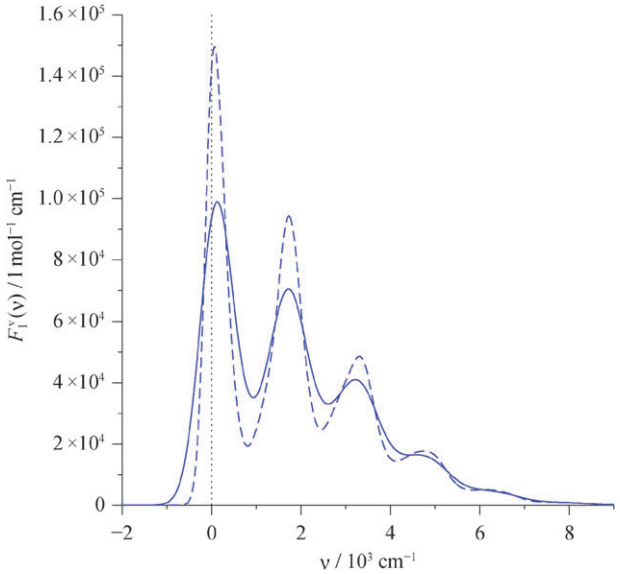

Fig. 7 Vibrational intensity distribution determined for *trans*-4-styrylpyridine (B3LYP/$\mathscr{G}$ results): the function $F_1^{\nu}(\nu)$ is plotted for an electronic transition energy of $\nu_1 = 0$ cm^{-1}, an oscillator strength of $f_1 = 1$, and using Gaussian convolution functions with FWHM of 400 cm^{-1} (dashed line) and 800 cm^{-1} (solid line).

at ~3400 cm^{-1} and ~2600 cm^{-1}, respectively. Note that these profiles globally hardly evolve on changing the FWHM of the Gaussians from 400 cm^{-1} to 800 cm^{-1}.

Finally, in order to take both the thermal broadening and the vibronic broadening into account, the main absorption bands of the two isomers have been calculated as time averages over the 300 K CPMD trajectories using eqn (4). Gaussians with FWHM value of 800 cm^{-1} were employed. Fig. 9 shows the predicted main absorption bands of the two isomers. In both cases, one notes that the calculated absorption bands are slightly shifted to higher energies. But, most importantly, one can note that the inclusion of the vibronic broadening clearly leads to a further improvement of the agreement between experiment and theory. Indeed, the shapes and the intensities of the calculated main absorption bands are in quite good agreement with their experimental counterparts, the agreement being far better than the one observed when including the thermal fluctuation effects only (Fig. 4).

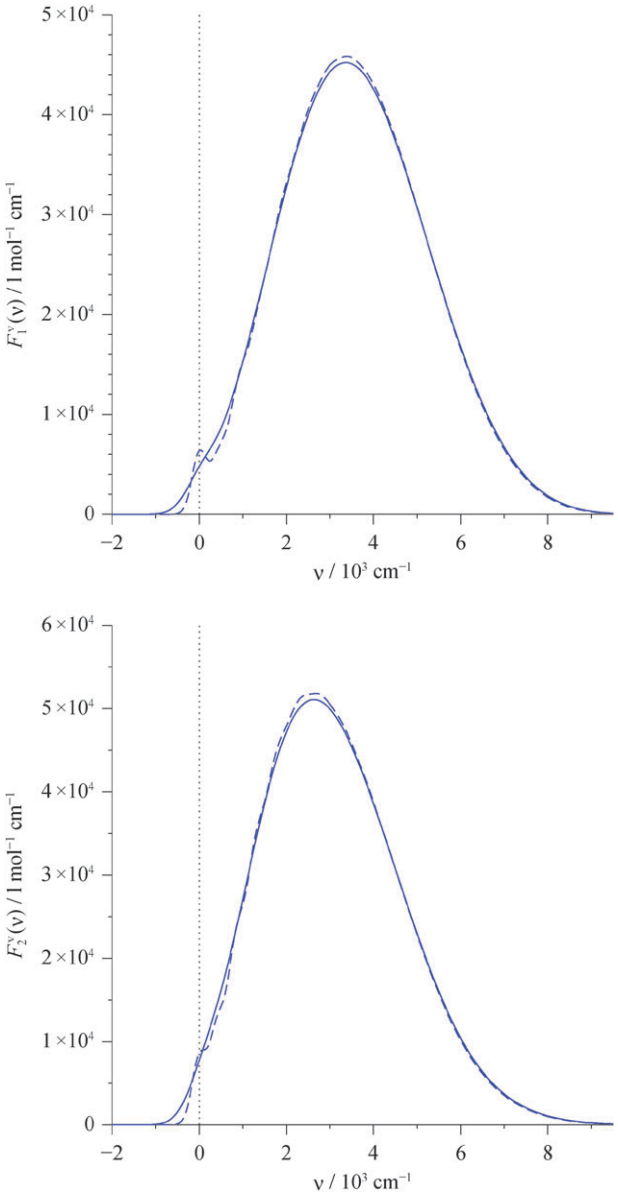

Fig. 8 Vibrational intensity distributions determined for *cis*-4-styrylpyridine (BOP/$\mathscr{G}$ results): the functions $F_I^{\nu}(\nu)$ ($I = 1,2$) are plotted for an electronic transition energy of $\nu_I = 0$ cm^{-1}, an oscillator strength of $f_I = 1$, and using Gaussian convolution functions with FWHM of 400 cm^{-1} (dashed line) and 800 cm^{-1} (solid line).

4. Concluding remarks

Electronic excitation calculations performed within LR-TDDFT allowed us to give a detailed analysis of the ground-state absorption spectra of the *cis* and *trans* isomers of 4-styrylpyridine. The results of the excitation calculations performed on the optimised geometries of the two isomers showed that their main absorption bands originate from the two lowest-lying transitions of π–π* and *n*–π* types. However, as required for a thorough analysis of the finite-temperature absorption spectrum of a highly flexible molecule such as 4-styrylpyridine, it proved necessary to take the influence of the thermal fluctuations into account. The absorption spectra were consequently also calculated as time averages over CPMD trajectories: this led to a significant improvement of the agreement between experiment and theory. In order to also take the vibrational broadening into account, the Franck–Condon factors of the relevant vibrations were calculated within the displaced harmonic oscillator approximation. Thermal and vibrational broadenings could thus both be taken into account for the calculation of the main absorption bands: this led to a further noticeable improvement of the agreement between experiment and theory.

The remaining discrepancies probably mainly originate from the neglect of the solvent effects in our study. For instance, let us recall that the calculated extinction coefficient is proportional to $1/n_{\mathrm{medium}}$, where n_{medium} is the refractive index of the medium (see, *e.g.*, ref. 56). For our study

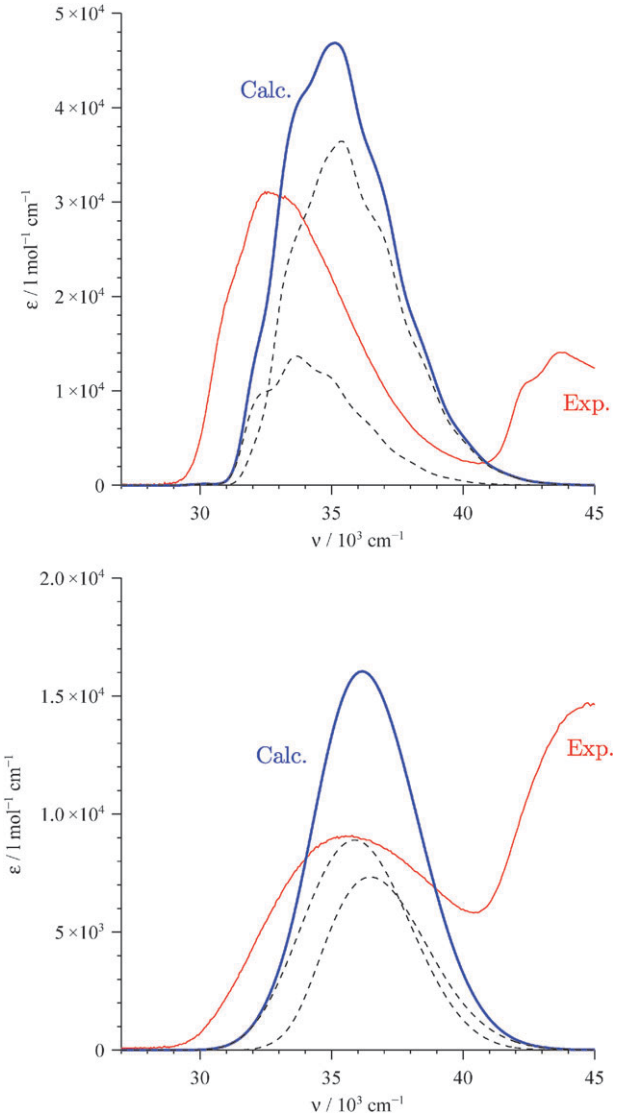

Fig. 9 Calculated 300 K main absorption bands (blue line) and experimental room-temperature absorption spectra (red line) of the *trans* (top) and *cis* (bottom) isomers of 4-styrylpyridine. The dashed lines corresponds to the calculated $S_0 \rightarrow S_I$ (I = 1,2) contributions to the main absorption bands.

performed in the gas phase, we used $n_{vacuum} = 1$. However, the experimental absorption spectra were recorded in methanol for which $n_{MeOH} \approx 1.3$. Thus, the division of the calculated absorption bands by n_{MeOH} provides a way to readily further improve the agreement between the intensities of the calculated and experimental absorption bands (Fig. 9). Still, the influence of the solvent must be addressed using a more complete approach. The solvent is indeed likely to affect the relative energies of the ground and excites states. Furthermore, the population distribution of either isomer along the relevant twisting angles $\phi_{Ph} = C_2–C_1–C_{Ph}–C_{o\text{-}Ph}$ and $\phi_{Py} = C_1–C_2–C_{Py}–C_{o\text{-}Py}$ is expected to be broader in a solvent than in the gas phase, because of the stabilisation of the twisted forms by the solute–solvent interactions. It thus follows that the absorption bands of the isomers can be expected to be broader and concomitantly less intense in the solvent than in the gas phase. Hence, in order to further improve our understanding of the optical properties of 4-styrylpyridine, it is necessary to extend the present study so as to explicitly take the influence of the solvent into account. This is work in progress.

Acknowledgements

This work has benefited from the financial support of the MAGMANet NoE of the European Union (contract NMP3-CT-2005-515767-2). This work was supported by a grant from the Swiss National Supercomputing Centre (CSCS) under project ID 103. L. M. L. D. thanks the University of Versailles for a guest professor position.

References

1 D. G. Whitten and M. T. McCall, *J. Am. Chem. Soc.*, 1969, **91**, 5097–5103.
2 G. Bartocci, P. Bortolus and U. Mazzucato, *J. Phys. Chem.*, 1973, **77**, 605–610.
3 G. Bartocci, U. Mazzuta, F. Masetti and G. Galiazzo, *J. Phys. Chem.*, 1980, **84**, 847–851.
4 U. Mazzucato, *Pure Appl. Chem.*, 1982, **54**, 1705–1721.
5 F. Barigelletti, S. Dellonte, G. Orlandi, G. Bartocci, F. Masetti and U. Mazzucato, *J. Chem. Soc., Faraday Trans. 1*, 1984, **80**, 1123–1129.
6 G. Marconi, G. Bartocci, U. Mazzucato, A. Spalletti, F. Abbate, L. Angeloni and E. Castellucci, *Chem. Phys.*, 1995, **196**, 383–393.
7 J. Otsuki, A. Suka, K. Yamazaki, H. Abe, Y. Araki and O. Ito, *Chem. Commun.*, 2004, 1290–1291.
8 H. Sugimoto, T. Kimura and S. Inoue, *J. Am. Chem. Soc.*, 1999, **121**, 2325–2326.
9 H. Sugimoto and S. Inoue, *Pure Appl. Chem.*, 1998, **70**, 2365–2369.
10 M.-L. Boillot, J. Zarembowitch and A. Sour, *Spin Crossover in Transition Metal Compounds II*, Springer-Verlag, Heidelberg, 2004, vol. 234, pp. 261–276.
11 C. Roux, J. Zarembowitch, B. Gallois, T. Granier and R. Claude, *Inorg. Chem.*, 1994, **33**, 2273–2279.
12 M.-L. Boillot, C. Roux, J.-P. Audière, A. Dausse and J. Zarembowitch, *Inorg. Chem.*, 1996, **35**, 3975–3980.
13 J. S. Kolb, M. D. Thomson, M. Novosel, K. Sénéchal, E. Rivière, M.-L. Boillot and H. Roskos, *C. R. Chim.*, 2007, **10**, 125–136.
14 M.-L. Boillot, S. Pillet, A. Tissot, E. Rivière, N. Claiser and C. Lecomte, *Inorg. Chem.*, 2009, **48**, 4729–4736.
15 *Spin Crossover in Transition Metal Compounds I*, ed. P. Gütlich and H. A. Goodwin, Springer-Verlag, Heidelberg, 2004, vol. 233.
16 *Spin Crossover in Transition Metal Compounds II*, ed. P. Gütlich and H. A. Goodwin, Springer-Verlag, Heidelberg, 2004, vol. 234.
17 *Spin Crossover in Transition Metal Compounds III*, ed. P. Gütlich and H. A. Goodwin, Springer-Verlag, Heidelberg, 2004, vol. 235.
18 P. Hohenberg and W. Kohn, *Phys. Rev.*, 1964, **136**, B864–B871.
19 W. Kohn and L. J. Sham, *Phys. Rev.*, 1965, **140**, A1133–A1138.
20 L. M. Lawson Daku, J. Linares and M.-L. Boillot, *ChemPhysChem*, 2007, **8**, 1402–1416.
21 R. Car and M. Parrinello, *Phys. Rev. Lett.*, 1985, **55**, 2471–2474.
22 E. Aprà, T. L. Windus, T. P. Straatsma, E. J. Bylaska, W. de Jong, S. Hirata, M. Valiev, M. Hackler, L. Pollack, K. Kowalski, R. Harrison, M. Dupuis, D. M. A. Smith, J. Nieplocha, V. Tipparaju, M. Krishnan, A. A. Auer, E. Brown, G. Cisneros, G. Fann, H. Früchtl, J. Garza, K. Hirao, R. Kendall, J. Nichols, K. Tsemekhman, K. Wolinski, J. Anchell, D. Bernholdt, P. Borowski, T. Clark, D. Clerc, H. Dachsel, M. Deegan, K. Dyall, D. Elwood, E. Glendening, M. Gutowski, A. Hess, J. Jaffe, B. Johnson, J. Ju, R. Kobayashi, R. Kutteh, Z. Lin, R. Littlefield, X. Long, B. Meng, T. Nakajima, S. Niu, M. Rosing, G. Sandrone, M. Stave, H. Taylor, G. Thomas, J. van Lenthe, A. Wong and Z. Zhang, *NWChem, A Computational Chemistry Package for Parallel Computers*, Version 4.7 Pacific Northwest National Laboratory, Richland, Washington 99352-0999, USA, 2005.

23 R. A. Kendall, E. Aprà, D. E. Bernholdt, E. J. Bylaska, M. Dupuis, G. I. Fann, R. J. Harrison, J. Ju, J. A. Nichols, J. Nieplocha, T. P. Straatsma, T. L. Windus and A. T. Wong, *Comput. Phys. Commun.*, 2000, **128**, 260–283.
24 M. E. Casida, *Recent Advances in Density Functional Methods, Part I*, World Scientific, Singapore, 1995, vol. 1, pp. 155–192.
25 S. Hirata, C.-G. Zhan, E. Aprà, T. L. Windus and D. A. Dixon, *J. Phys. Chem. A*, 2003, **107**, 10154–10158.
26 N. Godbout, D. R. Salahub, J. Andzelm and E. Wimmer, *Can. J. Chem.*, 1992, **70**, 560–571.
27 M. W. Schmidt, K. K. Baldridge, J. A. Boatz, S. T. Elbert, M. S. Gordon, J. H. Jensen, S. Koseki, N. Matsunaga, K. A. Nguyen, S. J. Su, T. L. Windus, M. Dupuis and J. A. Montgomery, *J. Comput. Chem.*, 1993, **14**, 1347–1363.
28 M. S. Gordon and M. W. Schmidt, *Theory and Applications of Computational Chemistry, the first forty years*, Elsevier, Amsterdam, 2005, ch. 41, pp. 1167–1189.
29 http://www.msg.chem.iastate.edu/GAMESS/GAMESS.html (accessed December 23, 2009).
30 M. Chiba, T. Tsuneda and K. Hirao, *J. Chem. Phys.*, 2006, **124**, 144106.
31 A. D. Becke, *J. Chem. Phys.*, 1993, **98**, 1372–1377.
32 A. D. Becke, *J. Chem. Phys.*, 1993, **98**, 5648–5652.
33 Gaussian NEWS, v. 5, no. 2, summer 1994, p. 2. "Becke3LYP Method References and General Citation Guidelines".
34 T. H. Dunning, Jr. and P. J. Hay, *Methods of Electronic Structure Theory*, Plenum Press, New York, 1977, pp. 1–27.
35 A. D. Becke, *Phys. Rev. A: At., Mol., Opt. Phys.*, 1988, **38**, 3098–3100.
36 T. Tsuneda, T. Suzumura and K. Hirao, *J. Chem. Phys.*, 1999, **110**, 10664–10678.
37 G. Black, J. Daily, B. Didier, T. Elsethagen, D. Feller, D. Gracio, M. Hackler, S. Havre, D. Jones, E. Jurrus, T. Keller, C. Lansing, S. Matsumoto, B. Palmer, M. Peterson, K. Schuchardt, E. Stephan, L. Sun, K. Swanson, H. Taylor, G. Thomas, E. Vorpagel, T. Windus and C. Winters, *Ecce, A Problem Solving Environmentfor Computational Chemistry Software Version 4.5.1*, Pacific Northwest National Laboratory, Richland, Washington 99352-0999, USA, 2007.
38 Jmol: an open-source Java viewer for chemical structures in 3D, http: //www.jmol.org (accessed September 2, 2009).
39 B. McMahon and R. M. Hanson, *J. Appl. Crystallogr.*, 2008, **41**, 811–814.
40 F. Della Sala, R. Rousseau, A. Görling and D. Marx, *Phys. Rev. Lett.*, 2004, **92**, 183401.
41 N. L. Doltsinis and M. Sprik, *Chem. Phys. Lett.*, 2000, **330**, 563–569.
42 L. Bernasconi, M. Sprik and J. Hutter, *J. Chem. Phys.*, 2003, **119**, 12417–12431.
43 L. Bernasconi, J. Blumberger, M. Sprik and R. Vuilleumier, *J. Chem. Phys.*, 2004, **121**, 11885–11899.
44 A. Brown, C. M. Kemp and S. F. Mason, *J. Chem. Soc. A*, 1971, 751–755.
45 According to the empirical law of Brown *et al.* for organic chromophores,[44] the FWHM of the Gaussian to be used for calculating the absorption band tied to a transition at energy ν is $7.5\sqrt{\nu[(\mathrm{cm}^{-1})]}$. The value of 1500 cm^{-1} chosen for the FWHM is therefore appropriate for the plots of the absorption spectra in the 30 000–45 000 cm^{-1} energy range of interest to us.
46 As a note of caution, we would like to emphasise that the use of longer trajectories and of thousands of sample configurations is actually needed to prove that the calculated room-temperature spectra are converged. This clearly is not feasible. However, as shown here, the calculations of electronic excitation spectra based on the recorded AIMD trajectories allowed us to gain deep insight into the finite-temperature optical properties of the investigated system.
47 N. A. Besley and N. L. Doltsinis, *J. Chem. Theory Comput.*, 2006, **2**, 1598–1604.
48 S. P. Kwasniewski, J. P. François and M. S. Deleuze.
49 C. Manneback, *Physica*, 1951, **17**, 1001–1010.
50 W. L. Smith, *J. Phys. B: At. Mol. Phys.*, 1969, **2**, 1–4.
51 K. Huang and A. Rhys, *Proc. R. Soc. London, Ser. A*, 1950, **204**, 406–423.
52 D. Braun, B. C. Titeca and A. Ceulemans, *J. Porphyrins Phthalocyanines*, 2001, **5**, 33–43.
53 J. Gierschner, H.-G. Mack, L. Lüer and D. Oelkrug, *J. Chem. Phys.*, 2002, **116**, 8596–8609.
54 W. Rettig and M. Dekhtyar, *Chem. Phys.*, 2003, **293**, 75–90.
55 J. Tatchen and E. Pollak, *J. Chem. Phys.*, 2008, **128**, 164303.
56 A. P. Shreve and R. A. Mathies, *J. Phys. Chem.*, 1995, **99**, 7285–7299.